# Starlight beneath the waves : in search of TeV photon emission from Gamma-Ray Bursts with the ANTARES Neutrino Telescope

Laksmana-Astraatmadja, T.

## Citation

Laksmana-Astraatmadja, T. (2013, March 26). *Starlight beneath the waves : in search of TeV photon emission from Gamma-Ray Bursts with the ANTARES Neutrino Telescope*. *Casimir PhD Series*. Retrieved from https://hdl.handle.net/1887/20680

**Author**: Astraatmadja, Tri Laksmana
**Title**: Starlight beneath the waves : in search of TeV photon emission from Gamma-Ray Bursts with the ANTARES Neutrino Telescope
**Issue Date**: 2013-03-26

# 7 *Simulation of the detector response to downgoing muons*

THIS CHAPTER will discuss the results of Monte Carlo simulations of the response of the ANTARES detector to downgoing muon signals. There are two reasons why this study is necessary: First, the photomultipliers (PMT) are pointing downward to optimize the detection of upgoing neutrino-induced muons, hence the detection efficiency of downgoing muons will be different. This will affect the energy threshold of muon detection as well as the angular resolution of the track reconstruction. Secondly, downgoing muon events in previous analyses are treated only as backgrounds and not as possible signal. In this work downgoing muon events are treated both as signal and background.

## 7.1 *Simulation chains*

HERE we are interested in how downgoing muons are seen by the detector. The simulations are thus performed in the environment around the detector. This volume is called the *can*, a cylindrical volume with the detector placed at the centre. The size of the can covers the detector with a margin of a few times the attenuation length of light. With this definition, the Čerenkov photons produced outside the can do not reach the PMTs and thus do not need to be simulated.

Muon tracks are generated with `gentra`, a simpler version of `genhen` (Bailey, 2002), developed specifically to generate single muon tracks coming from a fixed zenith distance. The muons are generated with initial positions at the surface of the can. The azimuthal directions are isotropic but directed towards the inside of the can, while the zenithal directions are according to the provided zenith distance range. It is also possible to generate zenithal directions for a single value of zenith distance.

The energy of the muons are generated according to the power-law spectrum $dN_\mu/d\epsilon_\mu \sim \epsilon_\mu^{-\alpha}$, where $\alpha$ is usually fixed to $\alpha = 2$. The generated energy range is between 10 GeV and 1 PeV. In the first part of the simulation, the zenith distance range is from $0^\circ$ (coming straight from the zenith) to $90^\circ$ (parallel to the horizon), equally divided into six bins each $15^\circ$ wide. For each zenith distance bin, $10^7$ muon tracks are generated. For convenience this data set will be referred to as SIMULATION 1.

The propagation of the muon towards the detector, the generation of Čerenkov photons, and the generation of hits recorded by the PMTs are simulated with the `km3` program (Navas & Thompson, 1999; Bailey, 2002). `km3` uses a modified version of the `MUSIC`[1] package (Antonioli et al., 1997) to propagate the muon. `MUSIC` simulates both the energy loss and multiple scattering, and treat all manners of muon interaction with matter as a stochastic processes. The tracking of every photon emitted is very inefficient, thus a set of tables is constructed by taking into account the absorption and scattering of light and storing the average photon fields produced by muons for various distances, positions, and orientations of the PMTs with respect to the track. The number of the hits and the times on the optical modules are then sampled from these tables.

The next step is then simulated with the `TriggerEfficiency` (de Jong, 2009) program. This program simulates the PMTs and data acquisition system. Optical background is also added, the rates can either be provided by the user or generated according to a Poisson distribution based on measured rates. The latter can be chosen when one is interested to reproduce the conditions of a specific data taking period. Signal and background hits are then generated by simulating the response of the PMTs such as TTS and electronic, the charge threshold, time integration, and dead time. The hits are then processed based on the filtering algorithm discussed in Section 6.6.1. The events used in this analysis are triggered with the 3N trigger. This trigger is not only the standard trigger that is always present in ANTARES data taking, but it also has a high purity, i.e. has a directional information which is important for sources with known directions such as GRBs.

In `TriggerEfficiency`, the random background hits are generated according to the normal distribution, its rate is set to 100 kHz. The number of triggered physics events for each zenith distance is shown in the 4th column of Table 7.1.

[1] MUon SImulation Code

| Zenith distance [°] | Can area [km$^2$] | $N_{\rm gen}$ | $N_{\rm phys}$ | $N_{\rm reco}$ | $N_{\rm reco}(\psi \leq 1°)$ |
|---|---|---|---|---|---|
| $0 \leq \theta \leq 15$ | 0.18 | $10^7$ | 34556 (0.35%) | 33308 (96.39%) | 3956 (11.88%) |
| $15 \leq \theta \leq 30$ | 0.22 | $10^7$ | 17979 (0.18%) | 17713 (98.52%) | 3887 (21.94%) |
| $30 \leq \theta \leq 45$ | 0.26 | $10^7$ | 17783 (0.18%) | 17659 (99.30%) | 5143 (29.12%) |
| $45 \leq \theta \leq 60$ | 0.27 | $10^7$ | 24982 (0.25%) | 24881 (99.60%) | 8376 (33.66%) |
| $60 \leq \theta \leq 75$ | 0.27 | $10^7$ | 42374 (0.42%) | 42279 (99.78%) | 16374 (38.73%) |
| $75 \leq \theta \leq 90$ | 0.25 | $10^7$ | 81080 (0.81%) | 80073 (98.76%) | 35772 (44.67%) |

Table 7.1: A summary of the simulation results. The can area used in each zenith distance bin is the median value of the can area for each muon track within the bin. $N_{\rm gen}$ is the number of generated muon tracks at the edge of the can. $N_{\rm phys}$ is the number of triggered events. $N_{\rm reco}$ is the number of tracks succesfully reconstructed by `aafit` algorithm, and $N_{\rm reco}(\psi \leq 1°)$ is the number of tracks reconstructed to better than 1° from its true direction. The percentages in shown in a column is calculated relative to the previous column.

The tracks are then reconstructed with the `aafit v0r9pre` algorithm, which employs the track reconstruction algorithm discussed in Section 6.6.3.

From the fitting result of `aafit` we can obtain the goodness-of-fit $\Lambda$, which is the fit likelihood per number of degrees of freedom. The direction of the reconstructed track in azimuth angle $\hat{\phi}$ and zenith distance $\hat{\theta}$ is obtained as well as the covariance matrix $\hat{\sigma}$. The difference between the true track direction and the reconstructed track direction can be calculated from the dot product of the direction vectors of the true muon directions and the reconstructed directions:

$$\begin{aligned} \cos\psi &= \mathbf{x}_{\rm true} \cdot \mathbf{x}_{\rm reco}, \\ &= x_{\rm true}x_{\rm reco} + y_{\rm true}y_{\rm reco} + z_{\rm true}z_{\rm reco}, \end{aligned} \tag{7.1}$$

where $\mathbf{x}_{\rm true} = \{x_{\rm true}, y_{\rm true}, z_{\rm true}\}$ and $\mathbf{x}_{\rm reco} = \{x_{\rm reco}, y_{\rm reco}, z_{\rm reco}\}$ are the direction vectors of respectively the true muon direction and the reconstructed muon direction.

From the error covariance matrix $\hat{\sigma}$ (Equation 6.22) we would

Table 7.2: A summary of the simulation results for the fixed zenith distance source.

| Zenith distance [°] | Can area [km$^2$] | $N_{\rm gen}$ | $N_{\rm phys}$ | $N_{\rm reco}$ | $N_{\rm reco}(\psi \leq 1°)$ |
|---|---|---|---|---|---|
| 0 | 0.14 | $10^7$ | 44654 (0.45%) | 43385 (97.16%) | 22357 (51.53%) |
| 15 | 0.20 | $10^7$ | 23496 (0.23%) | 22908 (97.50%) | 3446 (15.04%) |
| 30 | 0.24 | $10^7$ | 16499 (0.16%) | 16332 (98.99%) | 4301 (26.33%) |
| 45 | 0.27 | $10^7$ | 19889 (0.20%) | 19784 (99.47%) | 6213 (31.40%) |
| 60 | 0.28 | $10^7$ | 30997 (0.31%) | 30905 (99.70%) | 11070 (35.82%) |
| 75 | 0.27 | $10^7$ | 56895 (0.57%) | 56793 (99.82%) | 23622 (41.59%) |

then obtain the angular error estimate $\sigma_\psi$ (Equation 6.23).

It is assumed that the detector is running with all 12 lines operational, which means that it is assumed that the detector is running with full capacity.

TABLE 7.1 summarised the results after each stage of simulation is passed. The numbers suggest that less than $\sim 1\%$ of the generated events are actually detected and reconstructed. While this number look discouraging, a look at Figure 7.1 however indicate that the majority of the undetected events are low-energy muons with energy $\epsilon_\mu \lesssim 50$ GeV. This can thus be interpreted as the threshold energy of ANTARES for downgoing muons. As we can see in column 5, $\sim 99\%$ of the detected events can be reconstructed albeit with varying degree of qualities. Column 6 tells us the number of reconstructed tracks with accuracy $\psi \leq 1^\circ$. The percentage varies with zenith distance, i.e. the shallower the tracks, the better its reconstruction quality.

To simulate a GRB event, separate simulations have also been performed with `gentra`. The simulations generate muon tracks from a fixed zenith distance. Six cases of zenith distances are simulated, from $\theta = 0$ to $\theta = 75^\circ$, with $15^\circ$ intervals. The generated tracks are then processed using the same procedure. A summary of the simulation results is shown seen in Table 7.2. We will refer to this data set as SIMULATION 2.

## 7.2 Detector performance

SEVERAL aspects of the simulations pertaining to the performance of ANTARES will be discussed in this Section, namely the shape of the energy spectrum, the effects of quality cuts, and the effective areas.

### 7.2.1 The muon energy spectrum

FIGURE 7.1 depicts the muon energy spectrum for SIMULATION 1 at various stages of the simulation. As mentioned in Section 7.1, a minimum threshold at muon energy $\epsilon_\mu \sim 50$ GeV can be seen. The detection efficiency increases with energy and at TeV scale the majority of muon tracks can be succesfully reconstructed. The

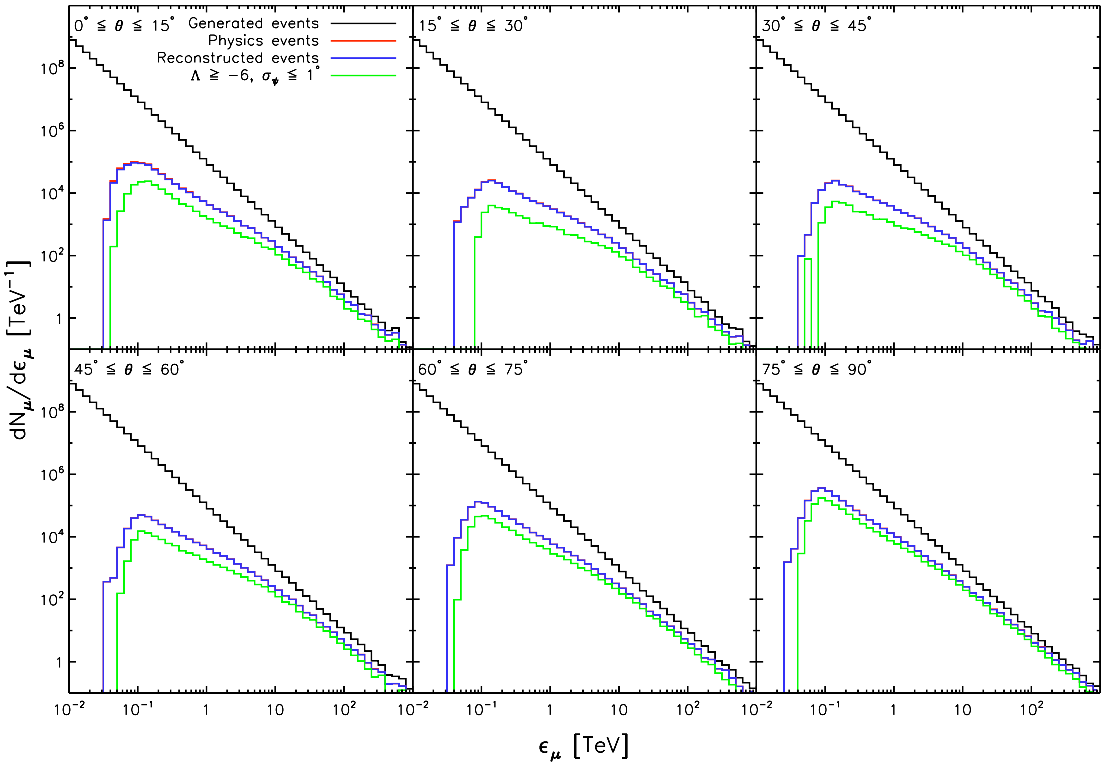

Figure 7.1: The development of the muon spectrum after each stage of the simulation. Black histogram shows the initial spectrum of the muons when they are generated with `gentra`, while red histogram corresponds to the events that pass the `TriggerEfficiency` program as triggered events. The dark blue histogram shows all events succesfully reconstructed by the `aafit v0r9pre` algorithm. The green histogram shows all events satisfying the quality cuts indicated at the legend.

plot of the muon detection efficiency $\eta_\mu$ as a function of muon energy $\epsilon_\mu$ is shown in Figure 7.8.

The shape of the reconstructed energy spectrum also varies with zenith distance bins. Except for the bins containing sources from the zenith, in general the detection efficiency increases with zenith distance. This effect could arise from the geometry of the detector. In the next section I will qualitatively discuss this relation between the detector geometry and the reconstruction quality.

### 7.2.2 *The quality of the reconstructed tracks and the preliminary cuts*

THE DISTRIBUTION of the true angular resolution $\psi$ (the difference between the reconstructed angle and the true angle), error estimate $\sigma_\psi$ (the statistical estimate of $\psi$), and the goodness-of-

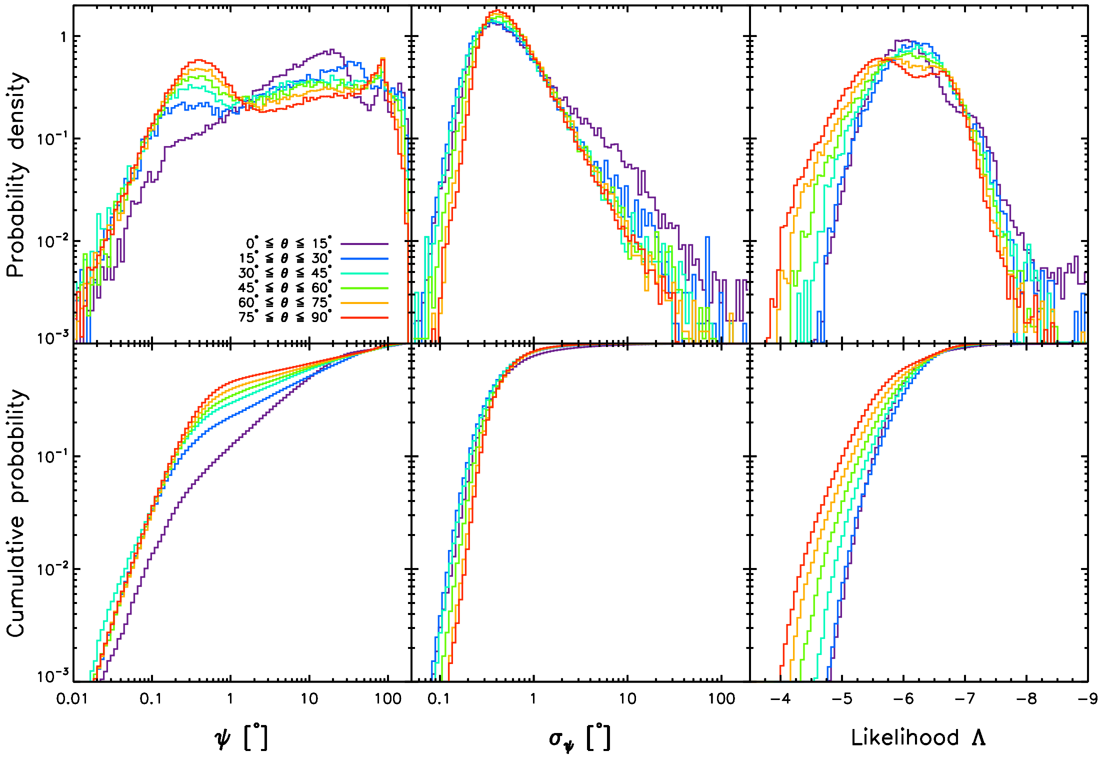

Figure 7.2: *Top:* The probability distribution function (PDF). *Bottom:* The cumulative distribution function (CDF). Both functions are shown for the true angular resolution $\psi$ (left), the angular uncertainty $\sigma_\psi$ (center), and the fit likelihood $\Lambda$ (right). Different color indicates different zenith distance according to the legend.

fit $\Lambda$ is shown in Figure 7.2 for all six cases of zenith distance bins. The top row plots the probability distribution function (PDF) while the bottom row plots the cumulative distribution function (CDF) of each parameter. Table 7.3 summarises the effects of quality cuts.

From Figure 7.2, we can see that for all bins, $\sim 80\%$ of all the muon tracks have an error estimate of $\sigma_\psi \lesssim 1^\circ$ (this can also be seen from column 3 in the top part of Table 7.3). The distribution of $\sigma_\psi$, however, does not completely reflect the distribution of $\psi$. As we can see in the left column of Figure 7.2 as well as the the rightmost column in Table 7.1, at best only $\sim 45\%$ of the reconstructed muon tracks (coming from zenith distances $75^\circ \leq \theta \leq 90^\circ$) are actually accurate to better than $1^\circ$, at worst only $\sim 12\%$ (coming from zenith distances $0^\circ \leq \theta \leq 15^\circ$). Thus

Table 7.3: A summary of the applied quality cuts. $N_{\text{reco}}$ is the number of tracks succesfully reconstructed by `aafit` algoritm and its percentage relative to $N_{\text{phys}}$. The first part of the table—under the first heading—shows the results of selecting reconstructed muon tracks with $\sigma_\psi \leq 1^\circ$. The second part under the second heading are for the results from selection of all tracks with $\Lambda_{\text{aafit}} \geq -6$, and the last part shows the results from selecting muon tracks with both quality: $\sigma_\psi \leq 1^\circ$ and $\Lambda_{\text{aafit}} \geq -6$. For each part, $N_{\text{sel}}$ is the number of tracks passing the applied quality cuts and its percentage relative to $N_{\text{reco}}$; $N_{\text{sel}}(\psi \leq 1^\circ)$ is the number of tracks with good accuracy (i.e. $\psi \leq 1^\circ$) and its percentage relative to $N_{\text{sel}}$; $N_{\text{sel}}(\psi > 1^\circ)$ is the number of poorly-reconstructed tracks and its percentage relative to $N_{\text{reco}}$; and finally $N_{\text{false}}$ is the number of false-negative tracks i.e. the number of tracks that did not get selected by the cuts even though they are accurately reconstructed to better than $1^\circ$. The percentage given in $N_{\text{false}}$ is relative to $N_{\text{reco}}(\psi \leq 1^\circ)$, shown in the rightmost column of Table 7.1.

| Zenith Distance | $N_{\text{reco}}$ | $N_{\text{sel}} = N_{\text{reco}}(\sigma_\psi \leq 1^\circ)$ | | | $N_{\text{false}}$ |
|---|---|---|---|---|---|
| | | $N_{\text{sel}}$ | $N_{\text{sel}}(\psi \leq 1^\circ)$ | $N_{\text{sel}}(\psi > 1^\circ)$ | |
| $0 \leq \theta \leq 15$ | 33308 | 25459 (76.44%) | 3602 (14.15%) | 21857 (85.85%) | 354 (8.95%) |
| $15 \leq \theta \leq 30$ | 17713 | 14665 (82.79%) | 3805 (25.95%) | 10860 (74.05%) | 82 (2.11%) |
| $30 \leq \theta \leq 45$ | 17659 | 14845 (84.06%) | 5018 (33.80%) | 9827 (66.20%) | 125 (2.43%) |
| $45 \leq \theta \leq 60$ | 24881 | 20691 (83.16%) | 8158 (39.43%) | 12533 (60.57%) | 218 (2.60%) |
| $60 \leq \theta \leq 75$ | 42279 | 35149 (83.14%) | 15874 (45.16%) | 19275 (54.84%) | 500 (3.05%) |
| $75 \leq \theta \leq 90$ | 80073 | 67746 (84.61%) | 34849 (51.44%) | 32897 (48.56%) | 923 (2.58%) |

| Zenith Distance | $N_{\text{reco}}$ | $N_{\text{sel}} = N_{\text{reco}}(\Lambda_{\text{aafit}} \geq -6)$ | | | $N_{\text{false}}$ |
|---|---|---|---|---|---|
| | | $N_{\text{sel}}$ | $N_{\text{sel}}(\psi \leq 1^\circ)$ | $N_{\text{sel}}(\psi > 1^\circ)$ | |
| $0 \leq \theta \leq 15$ | 33308 | 13916 (41.78%) | 3602 (25.88%) | 10314 (74.12%) | 354 (8.95%) |
| $15 \leq \theta \leq 30$ | 17713 | 5897 (33.29%) | 3399 (57.64%) | 2498 (42.36%) | 488 (12.55%) |
| $30 \leq \theta \leq 45$ | 17659 | 7045 (39.89%) | 4602 (65.32%) | 2443 (34.68%) | 541 (10.52%) |
| $45 \leq \theta \leq 60$ | 24881 | 11129 (44.73%) | 7652 (68.76%) | 3477 (31.24%) | 724 (8.64%) |
| $60 \leq \theta \leq 75$ | 42279 | 21661 (51.23%) | 15278 (70.53%) | 6383 (29.47%) | 1096 (6.69%) |
| $75 \leq \theta \leq 90$ | 80073 | 46705 (58.33%) | 34171 (73.16%) | 12534 (26.84%) | 1601 (4.48%) |

| Zenith Distance | $N_{\text{reco}}$ | $N_{\text{sel}} = N_{\text{reco}}(\sigma_\psi \leq 1^\circ, \Lambda_{\text{aafit}} \geq -6)$ | | | $N_{\text{false}}$ |
|---|---|---|---|---|---|
| | | $N_{\text{sel}}$ | $N_{\text{sel}}(\psi \leq 1^\circ)$ | $N_{\text{sel}}(\psi > 1^\circ)$ | |
| $0 \leq \theta \leq 15$ | 33308 | 11769 (35.33%) | 3317 (28.18%) | 8452 (71.82%) | 639 (16.15%) |
| $15 \leq \theta \leq 30$ | 17713 | 5573 (31.46%) | 3356 (60.22%) | 2217 (39.78%) | 531 (13.66%) |
| $30 \leq \theta \leq 45$ | 17659 | 6640 (37.60%) | 4516 (68.01%) | 2124 (31.99%) | 627 (12.19%) |
| $45 \leq \theta \leq 60$ | 24881 | 10484 (42.14%) | 7509 (71.62%) | 2975 (28.38%) | 867 (10.35%) |
| $60 \leq \theta \leq 75$ | 42279 | 20237 (47.87%) | 14912 (73.69%) | 5325 (26.31%) | 1462 (8.93%) |
| $75 \leq \theta \leq 90$ | 80073 | 43828 (54.74%) | 33432 (76.28%) | 10396 (23.72%) | 2340 (6.54%) |

between zenith distances of $0^\circ$ to $90^\circ$, the number of tracks accurately reconstructed to better than $1^\circ$ ranges from $\sim$12%–45%. This means that without any quality cuts, the majority of the reconstructed tracks actually have poor accuracy.

Another thing that we can see from the distribution of $\psi$ is that although a relatively large number of tracks coming from $0^\circ \leq \theta \leq 15^\circ$ can be successfully reconstructed compared to the following three zenith distance bins (see Column 5 in Table 7.1), almost 90% of them are actually poorly-reconstructed as compared to 70%–80% for the other bins. In other words, tracks coming from steep zenith distances (close to the zenith) can be efficiently reconstructed but with relatively low quality. This effect can be attributed to the geometry of the detector. More detector lines can participate in the detection of the Čerenkov photons when the muon passes the detector at a shallow angle, but only one or two detector lines participate in the detection when the muon is coming at a very steep angle. When only the PMTs from one or two lines detect photons, a symmetry in the data remains that results in an ambiguity of the track direction.

The relative number of poorly-reconstructed tracks could be reduced by applying selection cuts. The selection cuts are based on a combination of goodness-of-fit $\Lambda_{\text{aafit}}$ and angular resolution estimate $\sigma_\psi$. The distribution of $\psi$ are influenced by the combination of these two values.

We have seen that the angular error estimate $\sigma_\psi$ is not entirely correlated with $\psi$. This is more apparent in Figure 7.3, in which the 2 dimensional histogram of $\sigma_\psi$ and $\psi$ is shown. For all bins of zenith distance, if we select all tracks with $\sigma_\psi \leq 1^\circ$, we reject a large number of low-accuracy tracks. However, a considerable number of poorly-reconstructed tracks (with an angular deviation even as far as $180^\circ$) will contaminate the resulting subsample, assuming that the background distribution is approximately the same as the signal distribution. As we can see in Table 7.3, as much as $\sim 86\%$ and as little as $\sim 50\%$ of the subsample will still contain tracks with accuracy worse than $1^\circ$.

A tighter correlation exists between goodness-of-fit $\Lambda_{\text{aafit}}$ and $\psi$, as we can see in the 2D histogram of $\Lambda_{\text{aafit}}$ and $\psi$ shown in Figure 7.4. We can also see a progression of a bimodality in the dis-

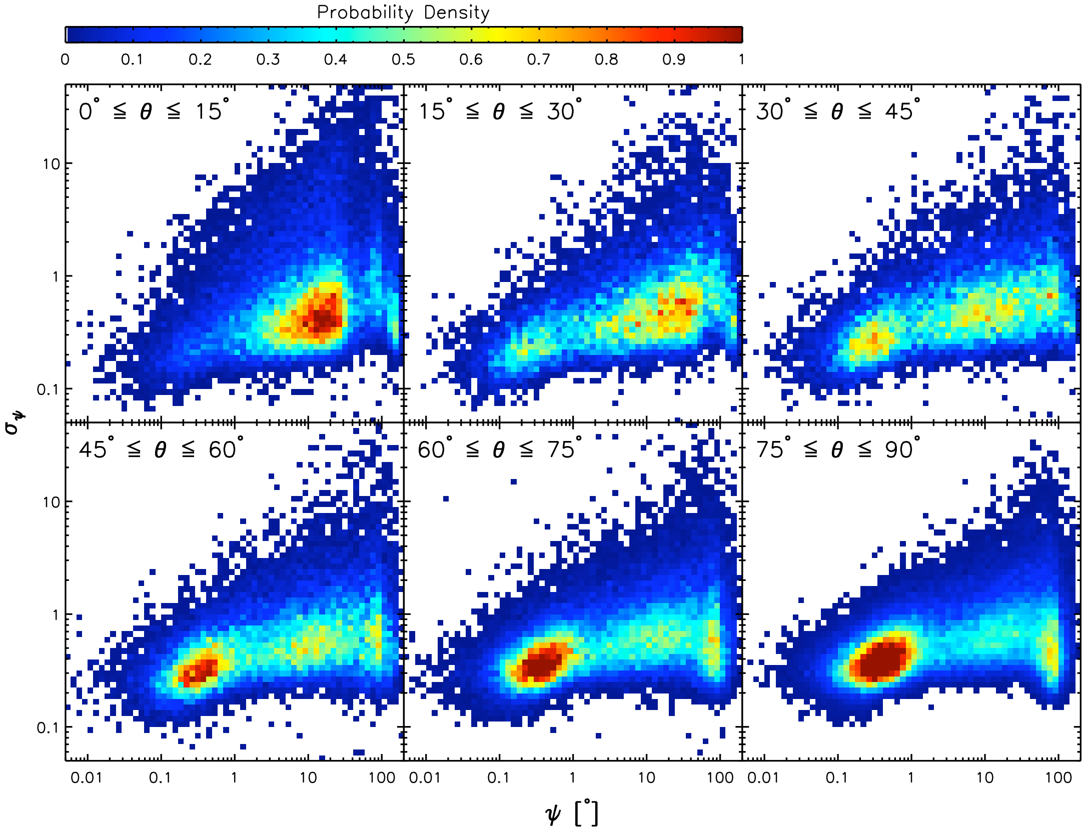

Figure 7.3: Two dimensional histogram of $\sigma_\psi$ and $\psi$. We can see that $\sigma_\psi$ is not entirely correlated with $\psi$. Tracks with estimated error $\sigma_\psi \leq 1°$ can actually be reconstructed with low accuracy, even as far as 180° from its actual direction.

tribution, in which there seems to be two peaks centered around $\psi \lesssim 1°$ and $\psi \sim 100°$. In zenith distance range $0° \leq \theta \leq 15°$, the distribution is concentrated at $(\psi, \Lambda_{\text{aafit}}) \sim (20°, -6.25)$. In general, the distribution of the good quality tracks is concentrated around $\Lambda_{\text{aafit}} \gtrsim -5.5$. If we accept all tracks with $\Lambda_{\text{aafit}} \geq -6$, we can obtain a good majority of the high-quality tracks while rejecting a considerable number of poorly-reconstructed tracks. In the middle part of Table 7.3, in Column 4, we can see that as much as $\sim 70\%$ of the high-quality tracks can be kept.

Having seen the effects of both quality cuts separately, we could also see their combined effects on the distribution of $\psi$. Such effects are shown in Figure 7.6, in which four combinations of qual-

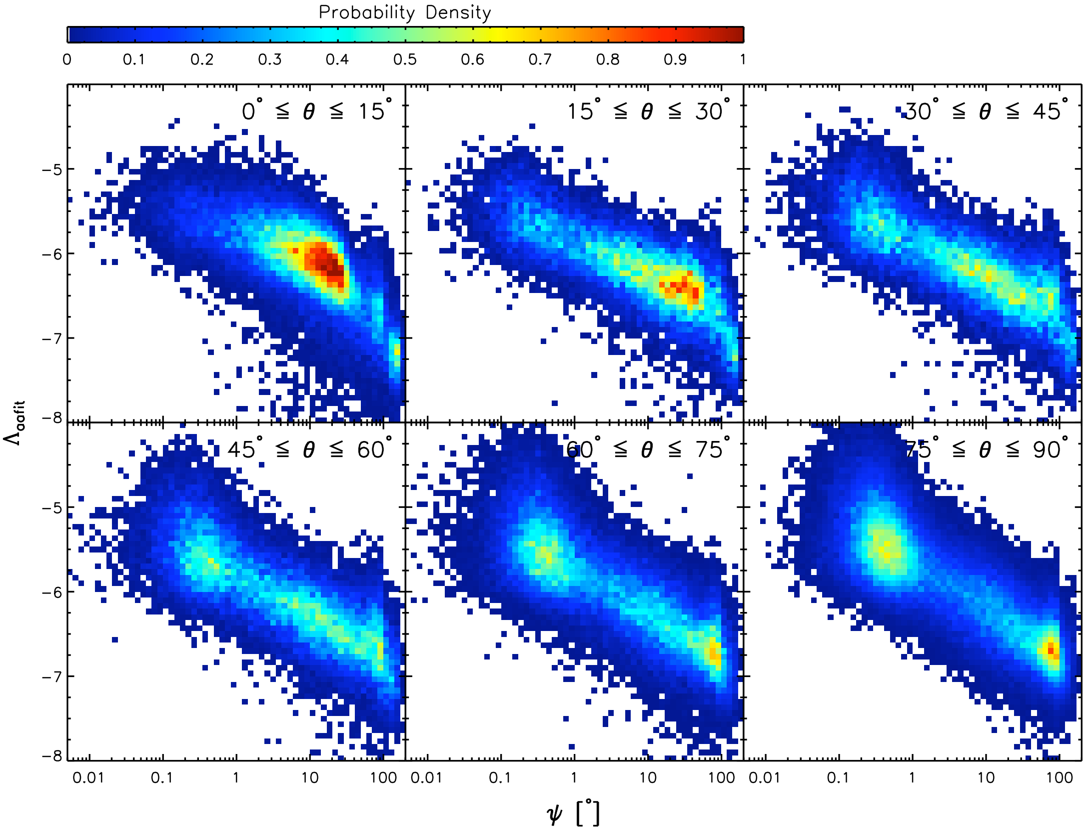

Figure 7.4: Two dimensional histogram of $\Lambda_{\text{aafit}}$ and $\psi$. A progression of a bimodality can be seen in the distribution with increasing zenith distance. The majority of tracks reconstructed to better than $1^\circ$ are concentrated above $\Lambda_{\text{aafit}} \sim -5.5$, while the poorly-reconstructed tracks (e.g. worse than $10^\circ$) are concentrated below $\Lambda_{\text{aafit}} \sim -6.5$.

ity cuts are considered, and their effects on the PDF and CDF of the true angular resolution $\psi$ are shown. With very loose quality cuts, shown as the purple-colored histogram, remains a considerable number of poorly-reconstructed tracks. With very tight quality cuts, shown as the red-colored histogram, a vast majority of the poorly-reconstructed muon tracks is rejected, but leaves only $\sim 10\%$ of all reconstructed events. This considerably decreases the detection efficiency.

Preliminary selection criteria of $\sigma_\psi \leq 1^\circ$ and $\Lambda_{\text{aafit}} \geq -6$ have been defined to compute the median accuracy of the reconstruction of downgoing muons. Figure 7.7 shows the cumulative distribution function of $\psi$ after such quality cuts are applied. Although

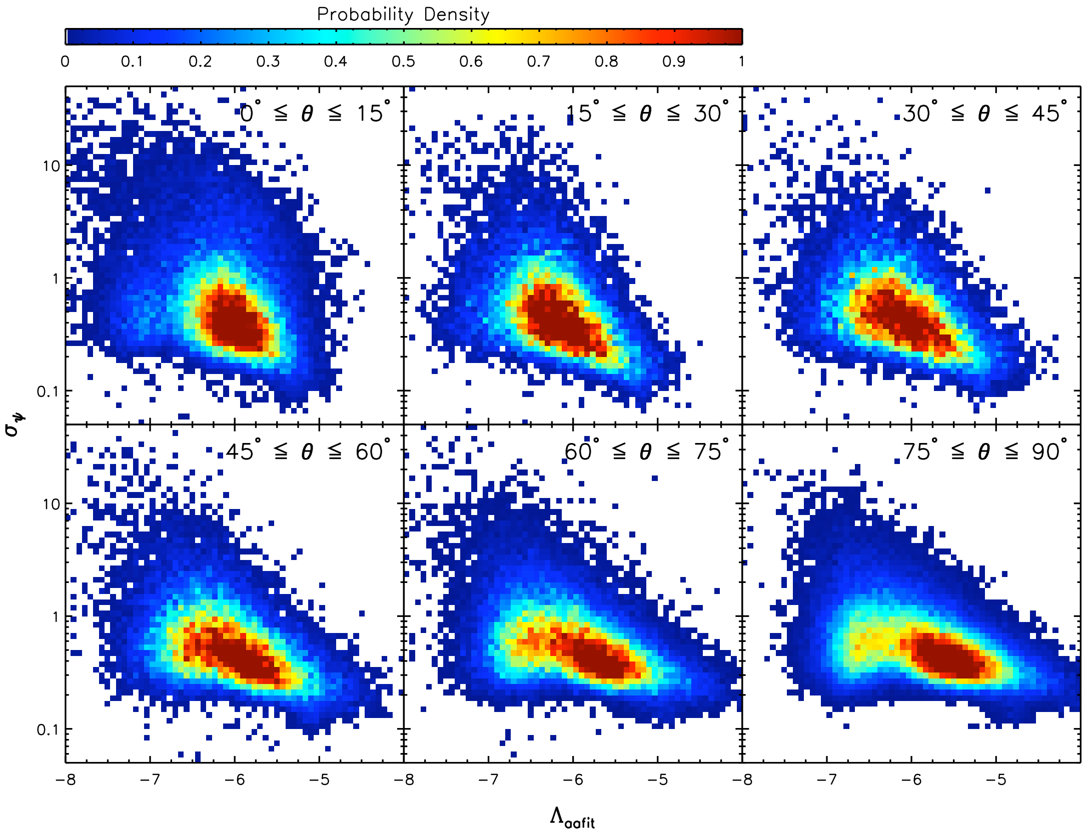

Figure 7.5: Two dimensional histogram of $\sigma_\psi$ and $\Lambda_{\mathrm{aafit}}$.

at steep zenith distances, i.e. $0^\circ \leq \theta \leq 15^\circ$, the median accuracy is $\psi \sim 3^\circ$, in general the median accuracy is $\psi \sim 0.4^\circ$.

The appropriate cut that could provide a good compromise between reliable background rejection and detector efficiency will be defined in Section 8.2, in which we include background data into the analysis.

### 7.2.3 *Effective areas*

The detection efficiency of the ANTARES detector as a function of energy, defined as the ratio between the number of recon-

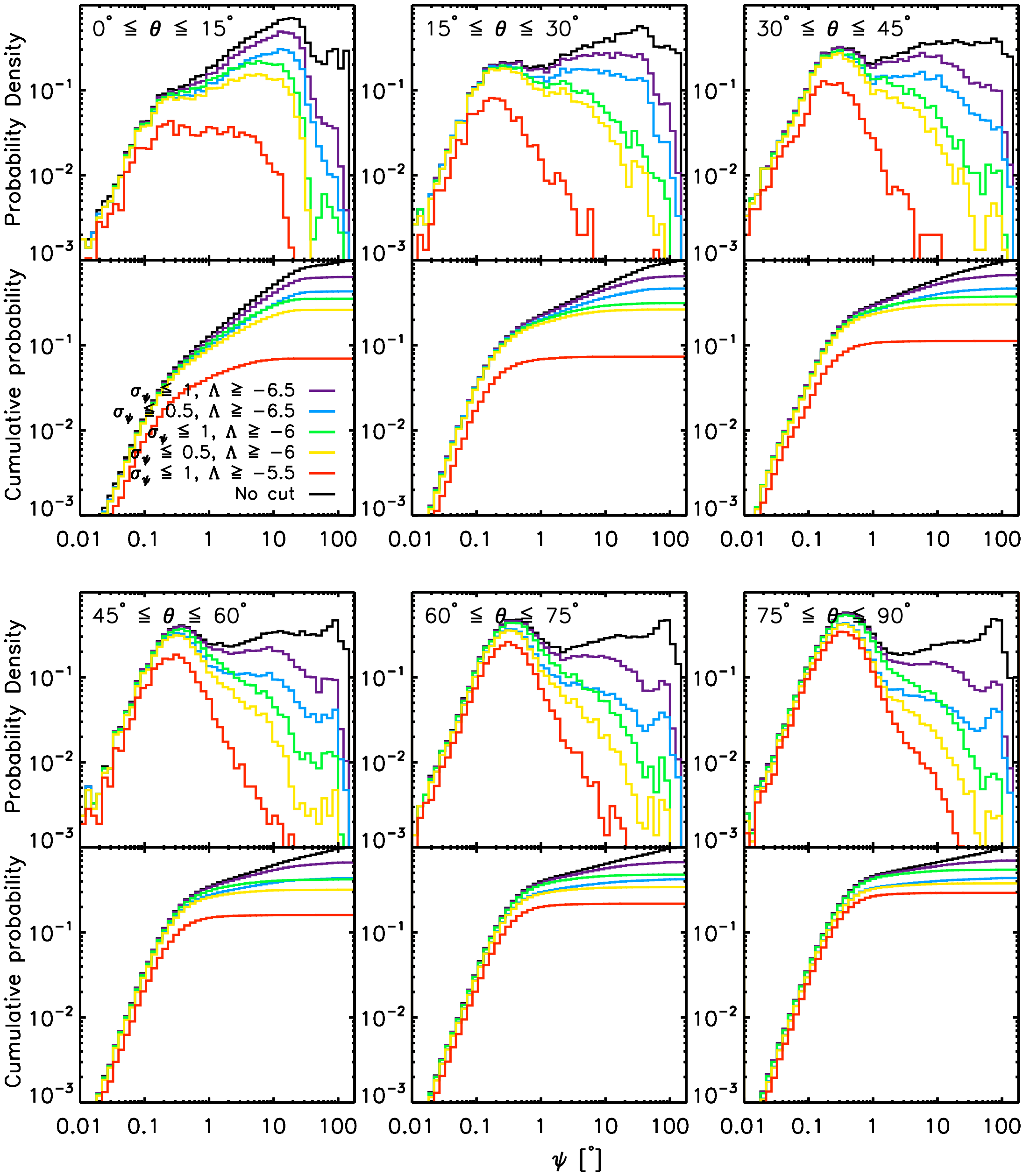

Figure 7.6: The effect of several quality cuts (indicated by different color coding shown in the legends) to the PDF and CDF of the angular resolution $\psi$.

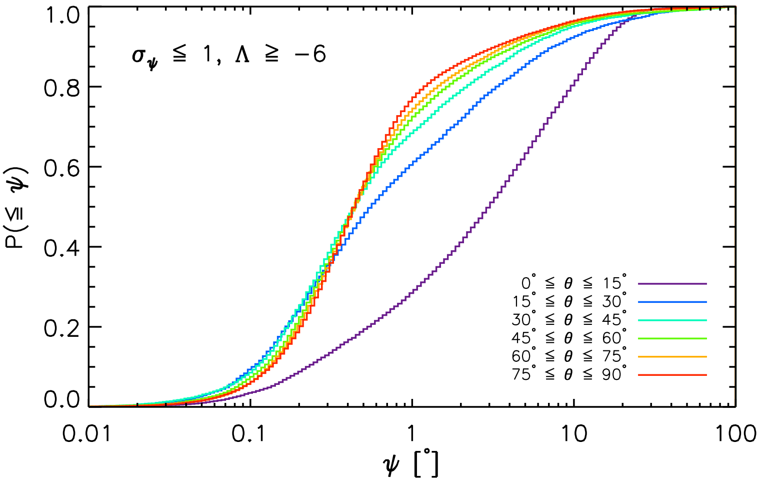

Figure 7.7: The CDF of the true angular resolution $\psi$ after the quality cuts $\sigma_\psi \leq 1^\circ$ and $\Lambda_{\text{aafit}} \geq -6$ have been applied. Only $\sim$ 30% of the signals coming from very steep zenith distances, $0^\circ \leq \theta \leq 15^\circ$, are going to be reconstructed to better than $1^\circ$, but other zenith distances will reconstruct to better than $1^\circ$ between $\sim$ 60–75% of the signals satisfying the applied cuts.

structed muon tracks and generated tracks in each energy bin,

$$\eta_\mu(\epsilon_\mu) = \frac{dN_{\mu,\text{rec}}}{dN_{\mu,\text{can}}}, \tag{7.2}$$

is shown in Figure 7.8. The top graphic depict the efficiency if all events are admitted while the bottom graphic is for all events satisfying the quality criteria $\sigma_\psi \leq 1^\circ$ and $\Lambda_{\text{aafit}} \geq -6$. The muon effective area $A_\mu^{\text{eff}}$ as a function of energy is also shown in Figure 7.8. The effective area is simply the detection efficiency multiplied by the generation area given in the second column of Table 7.1.

The muon detection efficiency and effective area for point sources corresponding to six considered cases of zenith distances (the SIMULATION 2 data set) are shown in Figure 7.9.

It is also possible to calculate the photon effective area $A_\gamma^{\text{eff}}$ as a function of the photon energy $\epsilon_\gamma$. First we must calculate the muon spectrum at the surface of the sea, assuming that the electromagnetic shower is initiated by a single photon with energy $\epsilon_\gamma$. The photon spectrum at the top of the atmosphere would then be

$$\gamma_0(\epsilon) = \gamma(\epsilon, t = 0) \equiv \delta(\epsilon - \epsilon_\gamma), \tag{7.3}$$

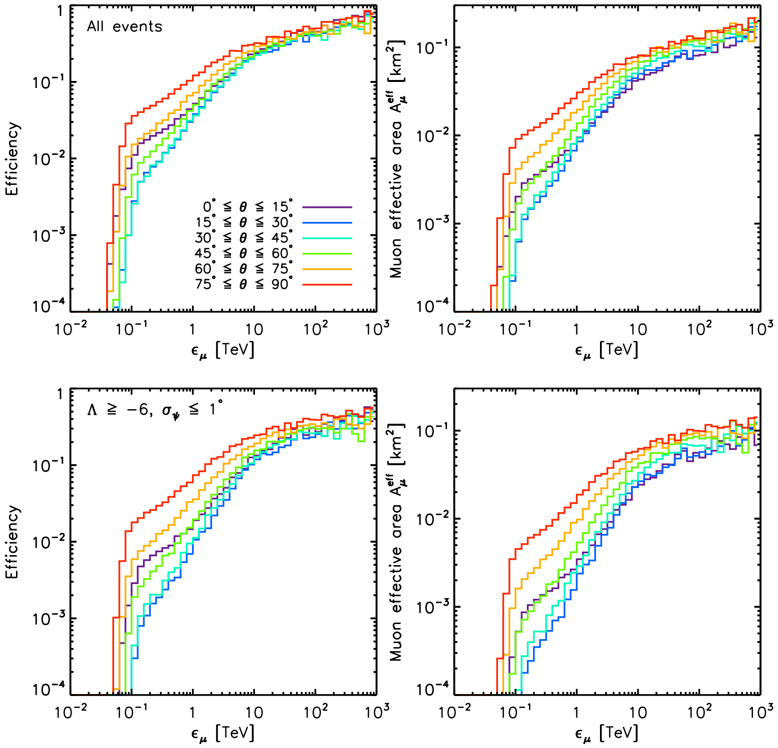

Figure 7.8: *Top:* The muon detection efficiency (left) and the muon effective area $A_\mu^{\mathrm{eff}}$ (right). *Bottom:* The same, but for events satisfying the quality cuts $\Lambda \geq -6$ and $\sigma_\psi \leq 1^\circ$. The efficiency and effective area are calculated using the data set in Simulation 1.

where $\delta$ is the Dirac delta function.

The development of the photon spectrum in the atmosphere could be determined using a discrete approximation, in which the atmosphere is segmented in layers if depth $\lambda_R \ln 2$ and that leptonic particles lose half their energy after passing each layer. At depth $t = n\lambda_R \ln 2$, the shower would contain $2^n/3$ photons with energy $\epsilon_\gamma/2^n$. This would mean that the shape of the photon spectrum at depth $t$ is

$$\gamma(\epsilon, t) = \frac{2^n}{3}\delta\left(\epsilon - \frac{\epsilon_\gamma}{2^n}\right). \tag{7.4}$$

Using this formula we could then calculate the muon flux from pair-production by using Equation 3.28, as well as the muon flux from pion decay (Drees, Halzen & Hikasa, 1989). The result of this analytical calculation is compared with results from `CORSIKA`

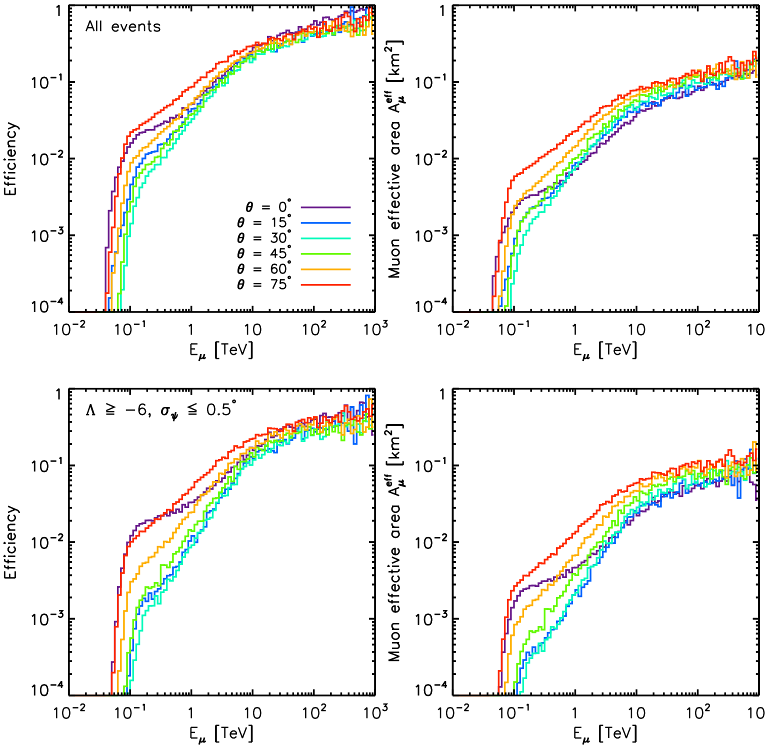

Figure 7.9: The same as in Figure 7.8, but for Simulation 2.

for a number of photons with energy $\epsilon_\gamma = \{1, 2, 5, 10, 50, 100\}$ TeV (Figure 7.10). We can see that there is a good agreement between theoretical calculations and the simulations. We can now calculate the muon spectrum at the detector using the manners described in Section 3.6. The muon spectrum at the detector, before and after reconstruction, is shown in Figure 7.11. Once we know the shape of the muon spectrum after reconstruction, it is straightforward to calculate the photon effective area. The photon detection efficiency would simply then be

$$\eta_\gamma(\epsilon_\gamma) = \frac{dN_{\mu,\rm rec}}{d\epsilon_\mu}. \tag{7.5}$$

The photon effective area $A_\gamma^{\rm eff}$ is then the photon detection efficiency multiplied by the generation area (column 2 in Table 7.2). The photon effective area as a function of energy is showed in

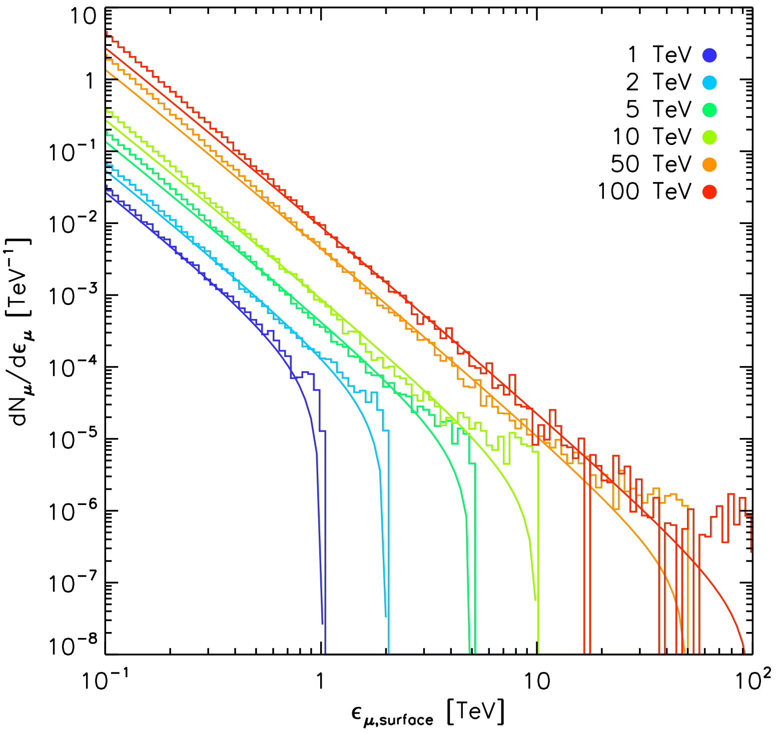

Figure 7.10: The muon flux at the sea surface, induced by single photons. The energy of the single photon is given in the legend. Results of the analytical calculations are also given as a comparison.

Figure 7.12. The photon effective area of other (spaceborne) $\gamma$-ray observatories is also shown for comparisons, namely *Fermi*-LAT, EGRET, and AGILE, which parameterization has been calculated by Le & Dermer (2009).

We can see that the photon effective area of ANTARES increases where other satellites are decreasing, thus complementing these instruments in higher energy ranges.

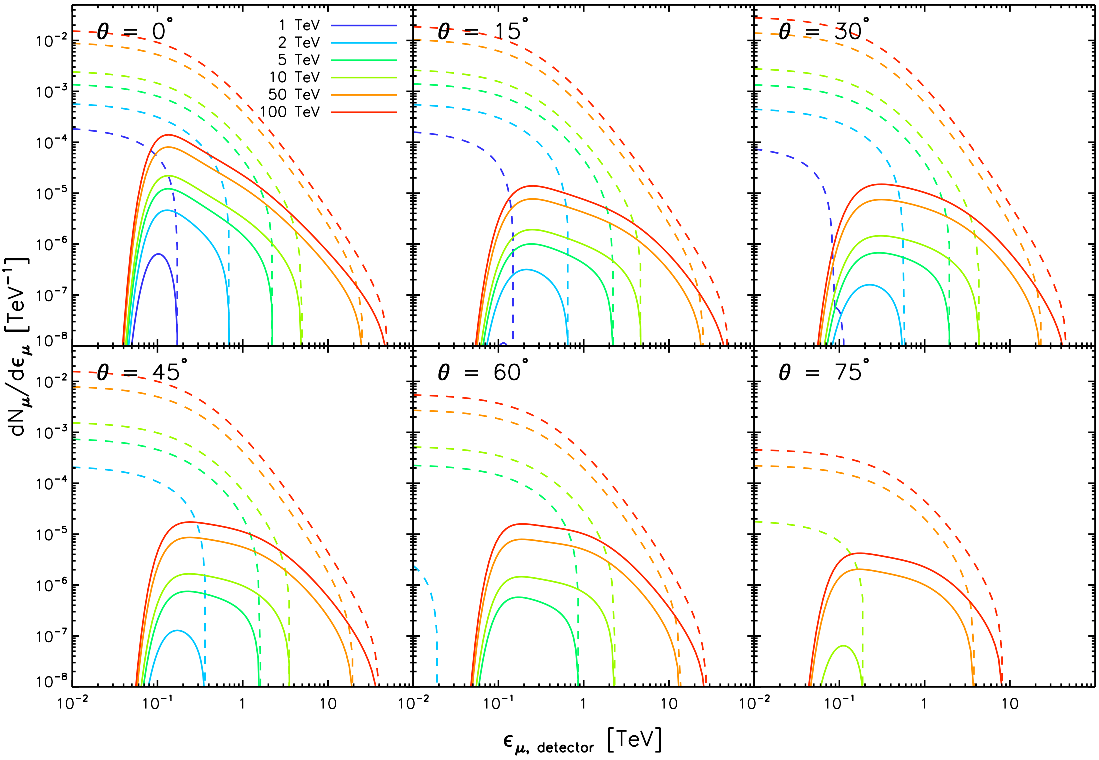

Figure 7.11: The shape of the muon spectrum induced by single photons, at detector level. The dashed lines are for spectrums of muons arriving at the detector, while the solid lines are after detection efficiency function is included. Each panel is for a different zenith distance.

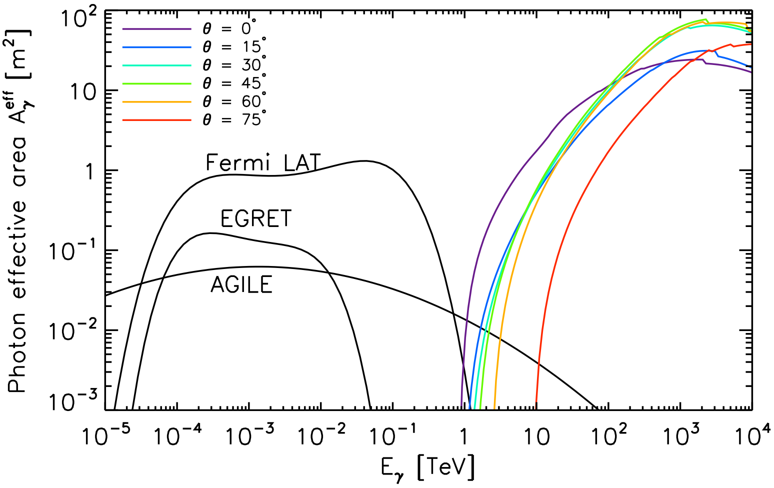

Figure 7.12: The ANTARES telescope photon effective area $A_\gamma^{\text{eff}}$ compared to space-borne $\gamma$-ray observatories.